Journal of Molecular Modeling (2023) 29:174
https://doi.org/10.1007/s00894-023-05584-7

ORIGINAL PAPER

Modeling stoichiometric and oxygen defective TiO_2 anatase bulk and (101) surface: structural and electronic properties from hybrid DFT

Zihan Wang[1] · **Frédéric Labat**[1]

Received: 1 March 2023 / Accepted: 5 May 2023 / Published online: 11 May 2023
© The Author(s), under exclusive licence to Springer-Verlag GmbH Germany, part of Springer Nature 2023

Abstract

Context We present a periodic hybrid DFT investigation of the structural and electronic properties of both stoichiometric and oxygen-defective TiO_2 anatase bulk and (101) surface, in singlet and triplet spin states. In all cases, an excellent agreement with available photoelectron spectroscopy data has been obtained, reproducing the offsets of the deep defect levels positions from the conduction band minimum of TiO_2 created upon oxygen vacancy (V_O) formation. For the bulk, different local structural polaronic distortions around the V_O site have been evidenced depending on the spin state considered. Although a similar conclusion has been drawn for the defective surface for the nine different vacancy positions which have been considered, large migration of the twofold coordinated surface O atom has also been evidenced, up to the initial vacancy site in some cases. The very good agreement obtained with available experimental data regarding the offsets from the conduction band minimum of the deep defect levels positions both for the bulk and the (101) surface of TiO_2 anatase is encouraging for the application of the proposed hybrid-based computational strategy to TiO_2 surface-related processes such as TiO_2-based photocatalysis in which oxygen vacancies are known to play a key role.

Methods All calculations have been performed with Crystal17, considering different hybrid functionals with both effective core pseudopotentials and all-electron atom-centered basis sets, as well as additional empirical dispersion effects with the D2 and D3 models.

Keywords TiO_2 · Defect · Surface · DFT

Introduction

While the properties of many materials are controlled by their geometries and electronic structures, defects can also play a key role in many of their applications [1–5]. Manipulating the nature and the concentration of defects by defect engineering is thus fundamental, albeit challenging, since this can indeed not only lead to tuned materials properties in a controlled way but also to completely new properties in some cases [6].

The importance of oxygen vacancies (V_O) as point defects in many metal oxides [5] has resulted in numerous investigations focusing at elucidating their role both experimentally and theoretically [3]. This is especially true for titanium dioxide (TiO_2), where V_O rather than Ti interstitials make the dominant contribution to the band gap states of TiO_2 surfaces [7]. With applications in various fields such as photocatalysis, solar cells, electronic devices, and environmental cleanup [8–15] for instance, TiO_2 is a technologically important material for which V_O play an important role in many of these applications. For instance, they were found not only to enhance the visible-light absorption of TiO_2 samples [16] but also to influence the adsorption and subsequent reactivity of molecules at TiO_2 surfaces [17–19], with possible important outcomes in photovoltaics and photocatalysis. Despite the larger thermodynamic stability of TiO_2 rutile compared to anatase, TiO_2 nanoparticles are common of the anatase type, with a higher efficiency in photocatalysis and photovoltaics than rutile [20–22], especially for its most reactive (001) and its most stable (101) surfaces. A better understanding of the role of V_O in TiO_2 anatase is therefore

✉ Frédéric Labat
frederic.labat@chimieparistech.psl.eu

[1] Chimie ParisTech, PSL University, CNRS UMR 8060, Institute of Chemistry for Life and Health Sciences, Theoretical Chemistry and Modeling Group, F-75005 Paris, France

crucial to better rationalize the defect engineering of such material.

From a modeling viewpoint, investigations dedicated to oxygen-defective TiO_2 have mainly been carried out at the density functional theory (DFT) level, using both spin-restricted and -unrestricted formalisms and a variety of DFT models [4, 23–34], although more advanced formalisms such as GW [35] have also been recently applied [36, 37]. Focusing on DFT investigations on anatase, a high sensitivity of the results to the DFT model has been evidenced both for the bulk [29] and for the defective (101) surface [34]. Cheng and Selloni showed that V_O are more stable subsurface than on the surface of anatase (101) using the generalized gradient approximation (GGA) [23], while a dependence of the relative stabilities of the surface and subsurface V_O could later be evidenced at the DFT+U level as a function of the U parameter value for the same surface [38]. The importance and stability of surface V_O was later confirmed with the hybrid HSE06 functional [39, 40] by Deák et al. [25] and Ha and Alexandrova [34] for instance, due to a possible interaction of the surface vacancy with a surface polaron [25]. In addition, the experimental spectral signature of reduced TiO_2 samples, with localized defect states at about 1.1 eV below the conduction band minimum (CBM) for TiO_2 anatase bulk [41] for instance, is not correctly reproduced by standard DFT models due to the overestimation of the delocalization of unpaired electrons and thus an underestimation of *d* electron localization in such models. A correct description indeed requires the use of either an on-site repulsion potential U with a sufficiently large, and potentially unphysical, value as in DFT+U approaches [38, 42–44] or of hybrid functionals [25, 32, 33]. These investigations have however generally considered different U values and/or different DFT models, supercell approaches with different supercell sizes, as well as singlet or triplet spin states, making a straightforward comparison of all computed data often difficult.

In this context, in this article, we present an investigation of stoichiometric and defective TiO_2 anatase bulk and (101) surface, considering different hybrid DFT functionals with both effective core pseudopotentials (ECP) and all-electron (AE) atom-centered Gaussian basis sets, along with both singlet and triplet spin states. For the defective (101) surface, nine different V_O positions have been considered. In all cases, we focus on local structural polaronic distortions around the V_O sites, and electronic structures description, especially regarding the positions of the deep defect levels in the TiO_2 band gap and the localizations of the excess electrons upon vacancy creation. This paper is organized as follows: in the "Computational details" section, we first introduce computational details, before presenting and discussing in the "Results and discussion" section the results obtained on stoichiometric and defective TiO_2, first for the bulk and then for the (101) surface. Finally, conclusions are drawn in the "Conclusions" section.

Computational details

All calculations have been performed with CRYSTAL [45, 46] which solves self-consistently both the Hartree-Fock and the Kohn-Sham equations as well as hybrid schemes, such as PBE0 [47] and HSE06 [39, 40], by expanding crystalline orbitals as a linear combination of atom-centered Gaussian type orbitals (GTO).

Five exchange-correlation functionals belonging to the GGA and hybrid families have been considered: PBE [48], PBE0 [47], B3LYP [49], B3PW [50], and HSE06 [39, 40]. Additional dispersive interactions have also been taken into account, using the empirical and semi-classical D2 and D3 corrections, as proposed by Grimme et al. [51, 52].

For all calculations, the ECP of Durand and Barthelat [53–55] have been combined into (1s1p5d)→[1s1p2d] and (4s4p)→[2s2p] contraction schemes for Ti and O [56], respectively, where the following cores have been used: Ti:(Ar) and O:(He). Additional AE basis sets with (20s,12p,4d)→[5s,4p,2d] and (14s,6p,1d)→[4s,3p,1d] contraction schemes [57] have also been used for Ti and O, respectively.

The infinite lattice sums of the Coulomb and exchange series were truncated with threshold values of 10^{-8}, 10^{-8}, 10^{-8}, 10^{-8}, and 10^{-24}, and numerical integration has been performed with 75 radial points and 974 angular points, ensuring an error on the integrated electron density to an accuracy of 10^{-5} e per cell [58].

All structures have been fully optimized, relaxing both atomic positions and cell parameters. Convergence was determined from the root-mean-square and absolute values of the largest component of the forces and displacements, considering default values [58].

To study neutral O vacancies, an unrestricted open-shell formalism has been considered throughout, both in singlet and triplet spin states, and spin contamination has been monitored by calculating the expectation value of S^2. Although the singlet open-shell case is not expected to be accurately described by a monodeterminental approach such as the one considered here, to allow for a straightforward comparison with previous works which have explored open-shell singlets at the DFT level [25, 32, 34, 37], a similar computational strategy has been considered here. Based on previous work [32], a (3×3×1) anatase bulk supercell of the conventional unit cell with 108 atoms was used. For the anatase (101) surface, a slab made of 12 Ti-layers, leading to converged surface properties, expanded in a (2×2) supercell with 144 atoms has been chosen. When creating an oxygen vacancy, the basis sets centered at the defect site have

been maintained in the calculation. Only the D2 approach has been considered in this case by setting the C_6 parameter related to V_O to zero. The oxygen vacancy formation energy (E_f^V) was computed with respect to the total energy of an oxygen molecule:

$$E_f^V = E(D) + \frac{1}{2}E\left(O_2\right) - E(H)$$

where $E(D)$ is the energy of the defective system, $E(O_2)$ is the energy of an O_2 molecule in its triplet ground state and $E(H)$ is the energy of the stoichiometric host material.

The reciprocal spaces have been sampled with (6×6×6) and (4×4×4) Monkhorst-Pack **k** point meshes [59], corresponding to 30 and 36 points in the irreducible Brillouin zones (IBZ) of stoichiometric and defective bulk anatase, respectively. For the anatase (101) surface calculations, a (4×4×1) *k*-point mesh has been used, corresponding to 7 **k** points in the IBZ of the (2×2) supercell considered.

Results and discussion

Bulk TiO_2

Stoichiometric bulk

Anatase has a tetragonal Bravais lattice with $I4_1/amd$ space group, whose conventional unit cell is shown in Fig. 1a. Table 1 presents computed lattice parameters and band gaps, using all combinations of DFT models and basis sets considered.

Clearly, all combinations perform well for the description of the a lattice parameter, with an error lower than 0.05 Å in all cases and only a very slight effect of dispersion effects no matter which dispersion model is considered. On the other hand, larger errors are usually obtained on the c lattice parameter, which might be related to the two axial Ti–O bonds along this direction. In particular, for all functionals,

Table 1 Computed data for stoichiometric bulk anatase with different functionals, considering both ECP and AE basis sets. Lattice parameters (a and c, in Å), oxygen fractional coordinate components (u) along c, and band gaps (E_g, in eV) are reported. The values given in parentheses correspond to band gaps computed with AE basis sets using ECP geometries

Method	Basis set	a	c	u	E_g
PBE	ECP	3.801	9.811	0.205	2.29 (2.37)
	AE	3.796	9.801	0.205	2.38
PBE-D2	ECP	3.780	9.823	0.205	2.30 (2.40)
	AE	3.776	9.806	0.205	2.41
PBE-D3	ECP	3.788	9.707	0.206	2.25 (2.35)
	AE	3.785	9.673	0.206	2.36
B3LYP	ECP	3.792	9.846	0.204	4.11 (4.01)
	AE	3.788	9.783	0.204	4.02
B3LYP-D2	ECP	3.763	9.866	0.204	4.15 (4.07)
	AE	3.759	9.799	0.204	4.07
B3LYP-D3	ECP	3.765	9.682	0.206	4.11 (4.04)
	AE	3.764	9.588	0.207	4.02
B3PW	ECP	3.771	9.845	0.204	3.89 (4.05)
	AE	3.769	9.701	0.205	4.06
B3PW-D2	ECP	3.741	9.878	0.203	3.93 (4.15)
	AE	3.740	9.727	0.205	4.15
B3PW-D3	ECP	3.745	9.655	0.206	3.88 (4.12)
	AE	3.745	9.480	0.208	4.08
HSE06	ECP	3.759	9.845	0.204	3.58 (3.91)
	AE	3.763	9.677	0.205	3.91
HSE06-D2	ECP	3.741	9.865	0.203	3.61 (3.96)
	AE	3.747	9.689	0.205	3.95
HSE06-D3	ECP	3.745	9.741	0.205	3.58 (3.95)
	AE	3.750	9.557	0.206	3.91
PBE0	ECP	3.759	9.837	0.204	4.16 (4.53)
	AE	3.764	9.665	0.205	4.53
PBE0-D2	ECP	3.741	9.858	0.203	4.18 (4.61)
	AE	3.748	9.675	0.205	4.60
PBE0-D3	ECP	3.745	9.746	0.205	4.15 (4.60)
	AE	3.749	9.565	0.206	4.59
Expt.		3.789[a]	9.522[a]	0.208[a]	3.18[b]

[a]from Ref. [61]; [b] from Ref. [62]

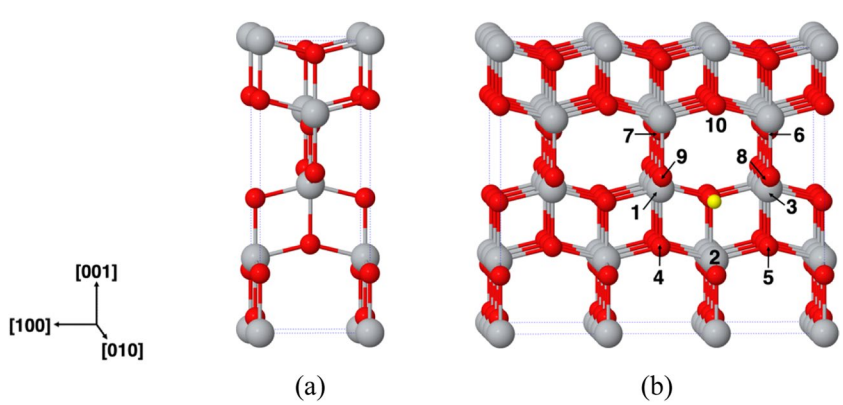

Fig. 1 **a** Conventional unit cell of bulk anatase, and **b** (3×3×1) supercell considered for the calculations of the defective bulk system. The unit cells are shown as blue dotted lines. Ti, O, and defective V_O sites are shown as grey, red, and yellow spheres, respectively

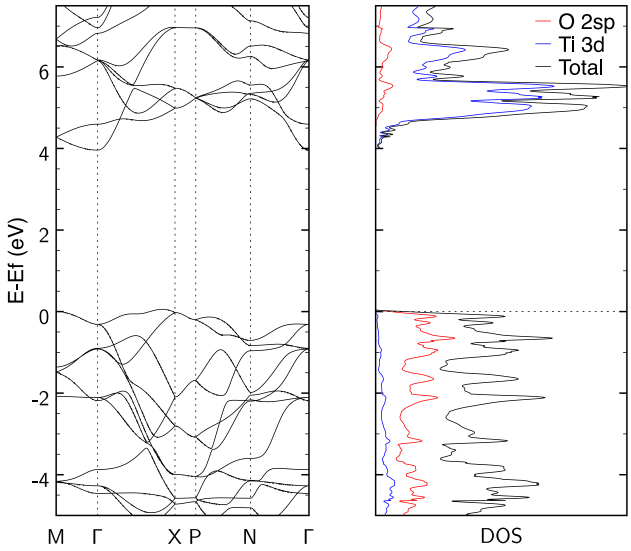

Fig. 2 Band structure, total and partial densities of states of stoichiometric bulk anatase obtained at the HSE06-D2 AE//ECP level. The Fermi level (shown as thin dotted line) has been set to 0 eV

the addition of D2 slightly increases c with respect to the corresponding value without dispersion, while D3 significantly decreases it with values computed approaching the experimental parameter. Overall, although the AE basis sets perform better for the structural description than the ECP ones, the performances of these latter remain acceptable. In addition, the D3 model always leads to a better agreement with the experimental data when compared to the bare DFT model, no matter which function is considered. The computed structures are in line with previously-reported GTO calculations [57, 60].

Regarding the computed band gaps, although the same qualitative picture is obtained in all cases, as already well-known, PBE tends to underestimate it while hybrids tend to overestimate it. Overall, the best agreement is obtained with the range-separated HSE06 functional, ECP basis sets leading to an artificially better agreement with the experimental value than the AE ones. Only a slight effect of the inclusion of dispersion effects can be evidenced for all DFT models considered. In addition, we note that computed band gaps with AE basis sets using ECP geometries (referred to

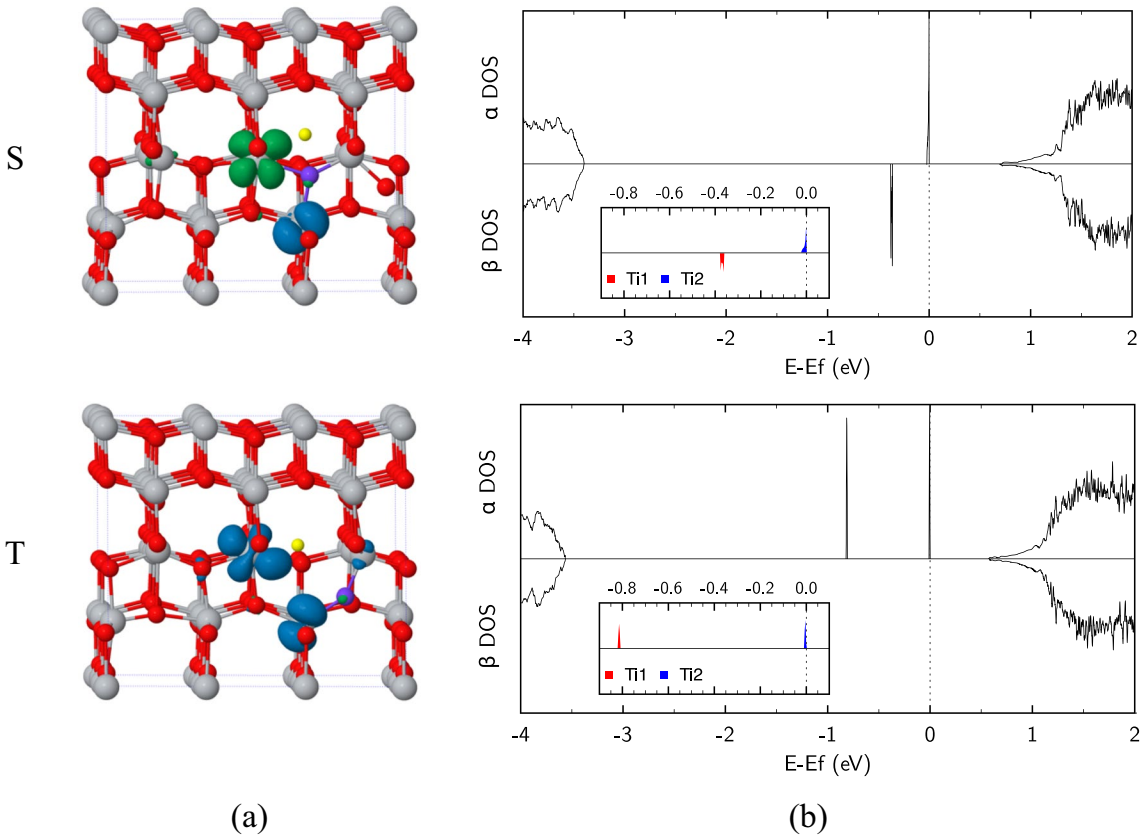

Fig. 3 **a** Fully relaxed structures along with computed spin densities, and **b** DOS and PDOS of bulk anatase (3x3x1) supercell with one V_O both in singlet (S) and triplet (T) spin states. All data obtained at the HSE06-D2 AE//ECP level. The Ti_1 and Ti_2 atoms correspond to the two Ti^{3+} sites where the excess electrons localize. The Fermi level has been set to 0 eV. For spin densities plots: isosurface values of |0.005| e.bohr^{-3}. Ti, O and defective V_O site shown as grey, red, and yellow spheres, respectively. The O_5 atom (see Fig. 1b) is highlighted in purple

Table 2 Selected distances (in Å) of stoichiometric and defective bulk anatase (3x3x1) supercell, considering both singlet (S) and triplet (T) spin states. All data obtained at the HSE06-D2 ECP level. See Fig. 1b for atom labeling.

	Stoichiometric			Defective					
				S			T		
	$d(Ti_1–Ti_3)$	$d(Ti_1–Ti_2)$	$d(Ti_3–Ti_2)$	$d(Ti_1–Ti_3)$	$d(Ti_1–Ti_2)$	$d(Ti_3–Ti_2)$	$d(Ti_1–Ti_3)$	$d(Ti_1–Ti_2)$	$d(Ti_3–Ti_2)$
This work	3.741	3.095	3.095	3.535	3.075	3.358	4.260	3.348	3.488
HSE/PAW[a]	3.77	3.06	3.06	3.87	3.22	3.22	-	-	-

[a](3×3×1) supercell, the two excess electrons are localized at the two first nearest neighbor Ti sites, from Ref. [32]. Only 20% of exact exchange at short-range

as AE//ECP level in the following and given in parentheses in Table 1) are very close to the AE data in all cases considered. This is especially true at the HSE06-D2 level, where only a 0.01 eV difference is obtained despite the ~ 0.2 Å difference obtained on the c lattice parameter. Since we found the large core pseudopotentials and related ECP basis sets not to be suitable to describe the electronic structures of defective systems, in the following, all calculations have therefore been performed at the HSE06-D2 AE//ECP level as a suitable compromise between accuracy and cost, considering the prohibitive computational costs of AE basis sets for the large supercells with low symmetry considered for defective systems.

The band structure, total and partial densities of states (DOS and PDOS) of stoichiometric bulk anatase computed at the HSE06-D2 level with AE basis sets using ECP geometries (referred to as HSE06-D2 AE//ECP level in the following) are shown in Fig. 2. The top of the valence band (VB) corresponds mainly to O-2sp states, with some slight contributions from Ti-3d states, while the bottom of the conduction band (CB) is largely composed of Ti-3d states. As already mentioned above, the computed indirect band gap between ~X and Γ of 3.96 eV is overestimated compared to the experimental value of 3.18 eV [62].

Overall therefore, for stoichiometric TiO_2 anatase, among the different combinations of DFT models and basis sets considered, the best results are obtained with the HSE06 functional, including dispersion effects (with D2 or D3 contributions) combined to AE basis sets. As mentioned above however, due to the prohibitive computational cost of AE basis sets for the comprehensive investigation of defective TiO_2 carried out below, single-point AE energies computed on ECP geometries (AE//ECP data) offer a suitable tradeoff between accuracy and computational costs. In addition, due to the form of the D3 contributions to the total energy, only the D2 dispersion model has been considered in all calculations including oxygen vacancies (see Computational Details for more details).

Defective bulk

The formation of one V_O leaves two excess electrons in the lattice which, according to experimental photoelectron spectroscopy (PES) data [41], localize at neighboring Ti sites at about 1.1 eV below the CBM, leading to Ti^{3+} species. Although different localization sites are possible (see Ref. 23, 29, 32 and for instance), in the following, we focus exclusively on the fully localized solutions on the two first nearest neighbor Ti atoms to the defective site, considering both

Table 3 Atomic displacements (in Å, from bulk-truncated positions) nearby the V_O site for the defective bulk anatase (3x3x1) supercell along different directions during geometry relaxation, both in singlet (S) and triplet (T) spin states. All data obtained at the HSE06-D2 ECP level. See Fig. 1b for atom labeling

Atoms	S			T		
	[100]	[010]	[001]	[100]	[010]	[001]
Ti_1	−0.12	0.06	−0.03	0.22	0.04	0.09
Ti_2	0.12	−0.03	−0.16	0.15	−0.01	−0.16
Ti_3	0.09	0.00	0.14	−0.29	0.02	−0.01
O_4	0.11	−0.03	−0.04	0.01	−0.01	0.08
O_5	1.65	−0.01	1.37	0.37	0.02	0.40
O_6	0.00	0.00	0.16	0.05	0.02	0.02
O_7	−0.03	0.00	0.13	0.19	0.01	0.17
O_8	−0.03	0.04	0.05	0.01	0.01	−0.02
O_9	−0.07	0.04	0.02	−0.06	0.04	0.02
O_{10}	−0.01	0.08	−0.02	0.06	0.04	−0.07

Table 4 Formation energies (E_f^V) of one V_O, band gaps (E_g) of α/β electrons, and offsets of the two deep defect levels (E_a and E_b) for the defective bulk anatase (3x3x1) supercell with respect to the CBM, along with the corresponding mean values (Ē), both in singlet (S) and triplet (T) spin states. All data (in eV) obtained at the HSE06-D2 AE//ECP level

	S					T				
	E_f^V	E_g	Offset from CBM			E_f^V	E_g	Offset from CBM		
			E_a	E_b	Ē			E_a	E_b	Ē
This work	6.55	0.71/1.09	1.09	0.71	0.90	6.74	0.57/4.14	1.39	0.57	0.98
HSE/PAW[a]	5.15	-	-	-	0.50	-	-	-	-	-
HSE/PAW[b]	5.33	-	-	-	0.50	-	-	-	-	-
B3LYP/GTO[c]	-	-	-	-	-	4.78	3.92	1.28	1.16	1.22
B3LYP/GTO[d]	-	-	-	-	-	4.84	3.92	1.35	0.59	0.97

[a](3x3x1) supercell, the two excess electrons are localized at the two first nearest neighbor Ti sites, from Ref. [32]. Only 20% of exact exchange at short-range.

[b]($2\sqrt{2}$x$2\sqrt{2}$x1) supercell, one excess electron localized at the first nearest neighbor Ti site, the other at the second nearest neighbor Ti site, from Ref. [25]

[c]($2\sqrt{2}$x$2\sqrt{2}$x1) supercell, one excess electron localized at the first nearest neighbor Ti site, the other at the second nearest neighbor Ti site, from Ref. [29]

[d]($2\sqrt{2}$x$2\sqrt{2}$x1) supercell, one excess electron localized at the first nearest neighbor Ti site, the other spreads over almost all of the Ti sites, from Ref. [29]

singlet (S) and triplet (T) spin states in a (3×3×1) supercell (see Fig. 1b). This is in line with a recent study suggesting the importance of Ti^{3+}–Ti^{3+} σ bond in defective TiO_2 [37]. The structures obtained after geometry optimization are shown in Fig. 3. Tables 2 and 3 report selected distances and atomic displacements nearby the V_O site after geometry relaxation, respectively, while relevant data regarding formation energies and electronic structures are collected in Table 4.

Significant differences have been obtained between the S and T solutions regarding the local structural polaronic distortions around the V_O site, with a larger asymmetry in the T case than in the S one. Indeed, while all the Ti–Ti distances reported in Table 2 for the T spin state are larger than those obtained for the stoichiometric systems, the S

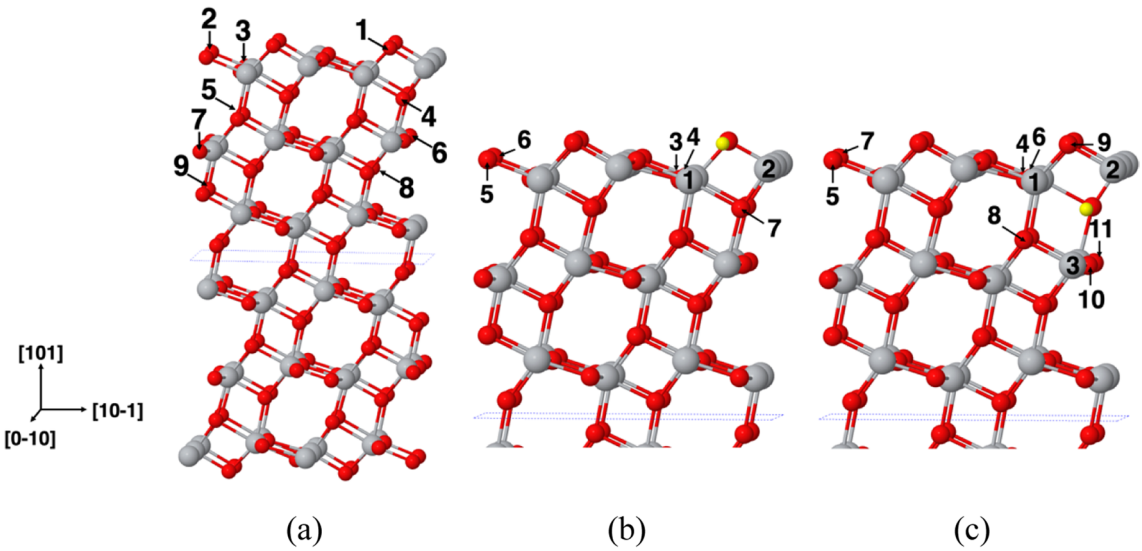

Fig. 4 **a** Anatase (101) slab model expanded in a (2×2) supercell with 12 Ti-layers showing V_O sites positions numbering (P1 to P9), and corresponding atom labelings of the **b** P1 and **c** P4 cases. The unit cell is shown as blue dotted lines. Ti, O, and defective V_O site shown as grey, red, and yellow spheres, respectively

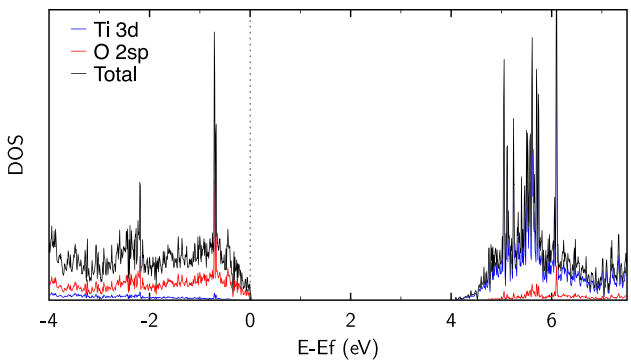

Fig. 5 Total and partial densities of states of the (2×2) supercell with 12 Ti-layers of anatase (101) computed at the HSE06-D2 AE//ECP level. The Fermi level (shown as thin dotted line) has been set to 0 eV

solution presents either smaller or larger values. In particular, all distances involving Ti_1 (see Fig. 1b) are smaller than in the stoichiometric case, while the Ti_3-Ti_2 one is larger. This can be related to the large displacements of the O_5 atom both in the [100] and [001] directions, which relaxes to almost occupy the original position of the V_O site, with a final computed d(Ti_1–O_5) value of 2.069 Å, that is about half of the one (3.977 Å) obtained in the T case. The computed distances reported in Table 2 are generally in qualitative agreement with a previous HSE/PAW investigation [32], although in this latter work: (i) no fully localized solution in the T spin state could be obtained, (ii) identical Ti_1–Ti_2 and Ti_3_Ti_2 distances were obtained, in clear contrast to our calculations where symmetry breaking around the V_O site occurs. According to the formation energies, E_f^V reported in Table 4, the S spin state is found about 0.2 eV more stable than the T one. We note that the E_f^V values obtained here are higher than those previously-reported at the HSE/PAW [32] or B3LYP/GTO [29] levels for instance, mainly due to the AE//ECP computational strategy adopted in our work. Nevertheless, based on the spin densities and densities of states reported in Fig. 3, we note that the two excess electrons left in the lattice by the neutral V_O localize almost exclusively at the two nearest-neighbor Ti sites Ti_1 and Ti_2, with absolute values of the magnetic moments of these atoms of at least 0.85 μ_B in all cases. In addition, based on the data reported in Table 4, when averaging the two Ti_1 and Ti_2 levels positions E_a and E_b in the DOS, offsets of 0.90 and 0.98 eV with respect to the CBM are obtained in the S and T spin states, respectively, in very good agreement with the 1.1 eV value reported experimentally by PES [41].

Finally, we note that the relaxed lattice parameters were found to be always within 1% of the stoichiometric values, indicating that the structural distortions around the V_O site are mainly due to strong local atomic relaxations rather than strong lattice relaxations. In addition, the spin contamination is high for the S state, while it is low for the T state, with computed expectation values of S^2 of 1.01 and 0.03 for the S and T solutions, respectively. While the former is related to the mono-determinantal nature of the approach considered, the low value obtained in the T case further confirms the validity of the solution obtained.

Anatase (101) surface

Stoichiometric surface

The anatase (101) surface is a stoichiometric non-polar surface with a characteristic sawtooth structure (see Fig. 4) with two and threefold coordinated O atoms (O_{2c} and O_{3c}) as well as five and sixfold coordinated Ti atoms (Ti_{5c} and Ti_{6c}). The computed surface energy of the (2×2) supercell considered with 12 Ti-layers is of 0.83 J/m^2 at the HSE06-D2 AE//ECP level, and 0.78 J/m^2 when fully relaxed at the HSE06-D2 AE

Table 5 Formation energies (E_f^V) of one V_O, band gaps (E_g) of α/β electrons, and positions of the two deep defect levels (E_a and E_b) for the defective (2×2) supercell of anatase (101) with respect to the CBM, along with the corresponding mean values ($\bar{E}$), both in singlet (S) and triplet (T) spin states, as a function of the V_O position (P). All data (in eV) was obtained at the HSE06-D2 AE//ECP level. The data obtained on the bulk system, already reported in Table 4, are also given

P	S					T				
	E_f^V	E_g	Offset from CBM			E_f^V	E_g	Offset from CBM		
			E_a	E_b	$\bar{E}$			E_a	E_b	$\bar{E}$
1	5.04	1.13/1.26	1.26	1.13	1.19	5.17	1.00/4.06	1.24	1.00	1.12
2	6.73	1.41/1.40	1.41	1.40	1.41	6.78	1.02/4.08	1.59	1.02	1.31
3	5.71	1.00/1.00	1.00	1.00	1.00	5.77	0.58/4.05	1.14	0.58	0.86
4	5.43	1.76/0.70	1.76	0.70	1.23	5.38	0.93/4.06	1.61	0.93	1.27
5	5.71	0.99/0.96	0.99	0.96	0.98	6.03	0.62/4.07	0.84	0.62	0.73
6	6.40	1.80/0.85	1.80	0.85	1.32	6.38	0.84/4.12	1.81	0.84	1.32
7	5.64	1.17/1.18	1.18	1.17	1.18	5.71	0.75/4.05	1.38	0.75	1.07
8	6.07	1.09/0.98	1.09	0.98	1.03	6.08	0.97/4.13	1.10	0.97	1.04
9	5.87	1.14/1.04	1.14	1.04	1.09	6.04	0.65/4.07	1.12	0.65	0.89
Bulk	6.55	0.71/1.09	1.09	0.71	0.90	6.74	0.57/4.14	1.39	0.57	0.98

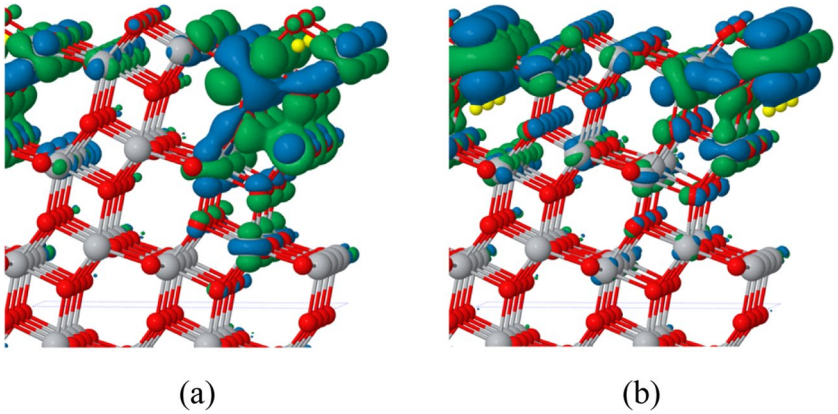

Fig. 6 α HOCO of the defective (2x2) supercell of anatase (101) with one V_O obtained in the S spin state for the **a** P1/(1/2;1/4) k point and **b** P4/(0;1/2) k point cases. Isosurface value of |0.02| $e^{1/2}.bohr^{-3/2}$. All data obtained at the HSE06-D2 AE//ECP level. Ti, O, and defective V_O site shown as grey, red, and yellow spheres, respectively

level. These values are in line with previously-reported ones obtained with various hybrid functionals with the same AE basis sets and the surface primitive cell [63]. In addition, the computed band gaps are 4.06 and 4.00 eV at the AE//ECP and AE levels, respectively, outlining the suitability of the computational strategy considered.

The computed DOS and PDOS shown in Fig. 5 are very similar to those previously discussed in the bulk case: the top of the VB corresponds mainly to O-2sp states, with some slight contributions from Ti-3d states, while the bottom of the CB is largely composed of Ti-3d states.

Defective surface

As already done in Ref. [34], nine different positions of the defective V_O sites have been considered (P1 to P9, see Fig. 4), going deeper and deeper in the slab, both in the S and T spin states. This allows to investigate surface (P1 to P3), subsurface (P4 to P6), and "bulk-like" (P7 to P9) vacancies. All optimized structures are shown in Figures S1 and S2 of the Supplementary Material, while relevant data regarding formation energies and electronic structures are collected in Table 5. As already done in the bulk case and supported by a recent study suggesting the importance of Ti^{3+}-Ti^{3+} σ bond in defective TiO_2 anatase (101) [37], we focus exclusively on fully localized solutions, that is solutions where the two excess electrons due to the V_O formation are localized on two first nearest neighbors Ti atoms of the V_O site.

Based on the data of Table 5, the S solution is generally found more stable than the T one like in the bulk, although differences remain generally small, with a maximal difference of formation energies lower than 0.3 eV among the different V_O positions considered. In addition, all computed values are lower than in the bulk case except the P2 case, in line with the importance of V_O in TiO_2 surface processes [18, 19]. More precisely, the E_f^V values range between 5.04 (at P1) and 6.73 eV (at P2) in the S case, while they range between 5.17 (at P1) and 6.78 eV (at P2). The relative stability order of the different V_O positions considered is the same in the S and T cases: P1 > P4 > P7 > P3 > P5 > P9 > P8 > P6 > P2. The greatest stability of the surface P1 position and the least stability of the surface P2 position are in line with recently-published data obtained in S spin state at the HSE06 level with ultra-soft pseudopotentials (USPP) [34], although the relative stability of the other positions differ. We note that this is also in agreement with recent a recent STM investigation which suggests that subsurface V_O clusters might convert to surface V_O for anatase (101) [64]. Figure 6 presents the computed highest occupied crystalline orbitals (HOCO) in the most stable S spin state for the two most P1 and P4 positions. The difference in stability between these two sites can be related to a fully bonding interaction between the *d* orbitals centered on Ti_1 and Ti_2 and the *p* orbitals of O_7 in P1, while a mixed bonding/antibonding character can be evidenced between the corresponding atoms in the P4 case.

As already found in the bulk case, we note that computed formation energies obtained in this work with the AE//

Table 6 Selected geometrical parameters of the defective anatase (101) (2x2) supercell with one V_O, both in singlet (S) and triplet (T) spin states. Distances (d) in Å and angles (θ) in degrees. All data obtained at the HSE06-D2 AE//ECP level. Atom labeling given in Fig. 4. The corresponding values of the stoichiometric (2x2) supercell are also reported

		Stoichiometric	Defective	
			S	T
P1	$d(Ti_1–O_7)$	2.113	2.012	2.036
	$d(Ti_2–O_7)$	1.726	1.853	1.787
	$θ(Ti_1–O_7–Ti_2)$	95.5	117.2	116.3
P4	$d(Ti_1–O_9)$	1.799	1.874	1.798
	$d(Ti_2–O_9)$	1.848	2.188	2.224
	$θ(Ti_1–O_9–Ti_2)$	103.0	131.2	132.7

Table 7 Atomic displacements (in Å, from relaxed stoichiometric supercell positions) around defective sites P1 and P4 for the (2×2) supercell of the anatase (101) surface with one V_O, considering both single (S) and triplet (T) spin states. All data obtained at the HSE06-D2 ECP level. See Fig. 4 for atom labeling

Atom	S			T		
	[010]	[-101]	[101]	[010]	[-101]	[101]
P1						
Ti_1	0.00	0.21	−0.28	0.00	0.23	−0.28
Ti_2	0.00	−0.23	−0.21	0.00	−0.15	−0.15
O_3	0.00	0.00	0.15	0.00	0.01	0.17
O_4	0.00	0.00	0.15	0.00	0.01	0.17
O_5	0.02	−0.04	−0.02	0.06	−0.06	0.06
O_6	−0.02	−0.04	−0.02	−0.06	−0.06	0.06
O_7	0.00	0.20	−0.01	0.00	0.18	0.04
P4						
Ti_1	0.00	0.30	−0.38	0.00	0.34	−0.37
Ti_2	0.00	−0.20	0.06	0.00	−0.15	0.06
Ti_3	0.00	0.02	0.20	0.00	0.02	0.19
O_4	−0.01	0.06	0.13	−0.02	0.04	0.15
O_5	0.02	−0.01	0.12	0.07	−0.06	0.14
O_6	0.01	0.06	0.13	0.02	0.04	0.15
O_7	−0.02	−0.01	0.12	−0.07	−0.06	0.14
O_8	0.00	0.23	0.02	0.00	0.22	0.04
O_9	0.00	−0.33	−1.95	0.00	−0.37	−1.93
O_{10}	0.01	0.00	0.13	0.01	−0.01	0.15
O_{11}	−0.01	0.00	0.13	−0.01	−0.01	0.15

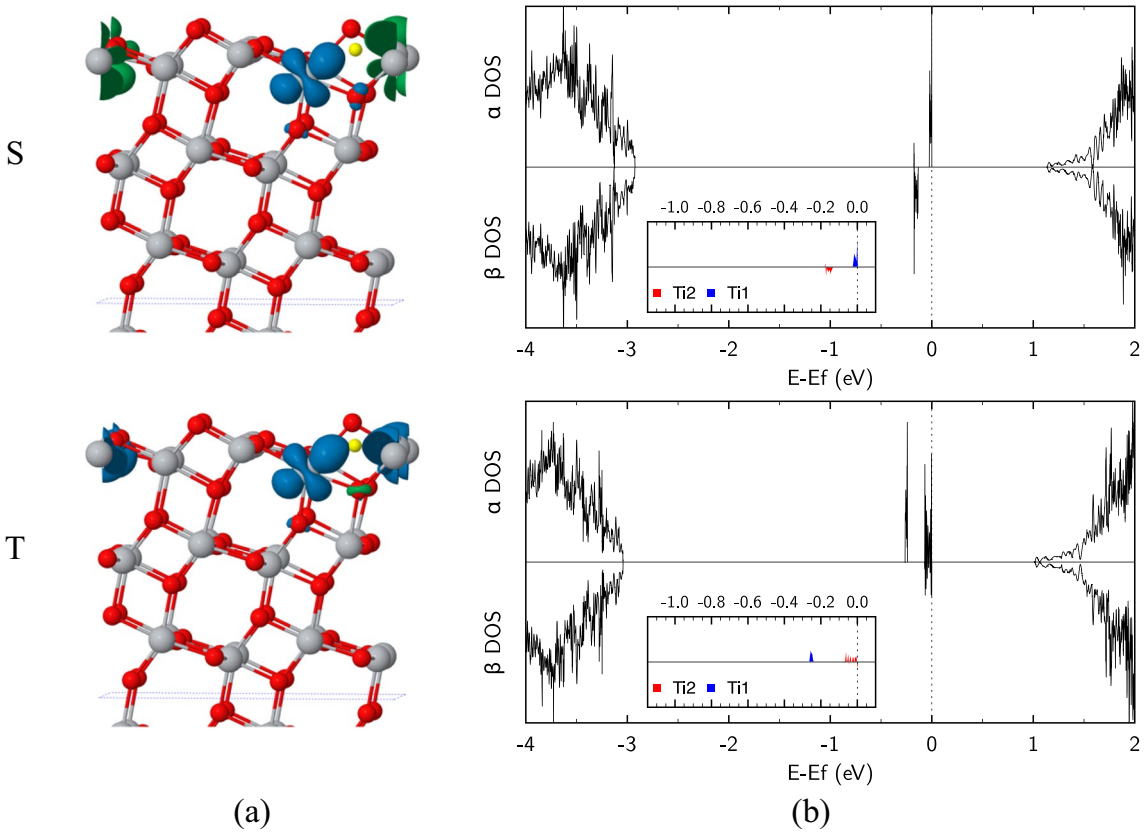

Fig. 7 **a** Computed spin densities, and **b** DOS and PDOS of the (2×2) supercell of anatase (101) with one V_O at position P1 in singlet (S) and triplet (T) spin states. All data obtained at the HSE06-D2 AE// ECP level. The Ti_1 and Ti_2 atoms correspond to the two Ti^{3+} sites where the excess electrons localize. The Fermi level has been set to 0 eV. For spin densities plots: isosurface values of |0.005| e.bohr^{-3}. Ti, O, and defective V_O site shown as grey, red, and yellow spheres, respectively

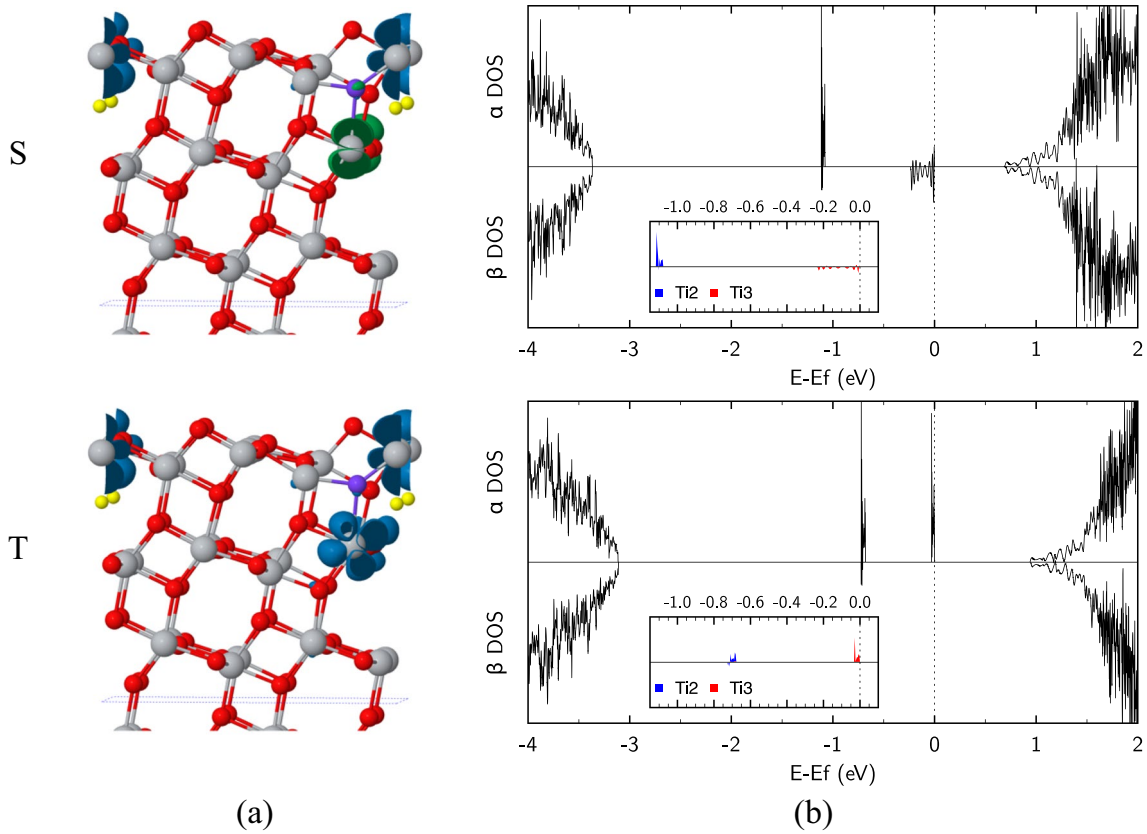

Fig. 8 **a** Computed spin densities, and **b** DOS and PDOS of the (2×2) supercell of anatase (101) with one V_O at position P4 in singlet (S) and triplet (T) spin states. All data obtained at the HSE06-D2 AE// ECP level. The Ti_2 and Ti_3 atoms correspond to the two Ti^{3+} sites where the excess electrons localize. The Fermi level has been set to 0 eV. For spin densities plots: isosurface values of |0.005| e.bohr^{-3}. Ti, O, and defective V_O site shown as grey, red, and yellow spheres, respectively. The O_9 atom (see Fig. 4c) is highlighted in purple

ECP strategy are overestimated compared to published data. Depending on the reference values considered, however, this overestimation is more or less important. For instance, at the HSE06/USPP level, Ha and Alexandrova [34] reported significantly different V_O formation energies of 2.91, 3.41, and 3.30 eV at the P1, P4, and P5 positions, respectively, while Deák et al. [25] reported values of 4.81, 5.03, and 5.46 eV, in much better agreement with the values reported in Table 5. Nevertheless, we note that in these two previous works and the work presented here, the surface vacancy position P1 is found to be the most stable one.

In all T cases considered, the two reduced Ti^{3+} sites contribute to the DOS at different offsets from the CBM (see E_a and E_b values, Table 5), as already found in the bulk case. On the other hand, in the S case, only the P4 and P6 cases lead to Ti^{3+} contributions at significantly different offsets. This can be related to a much larger structural distortion in these latter two cases than in the other ones. For instance, from Table 6 where some relevant geometrical parameters of the two most stable cases P1 and P4 are reported, we can note the larger distortion around the V_O site in the P4 case compared to the P1 one. This is confirmed by the computed atomic displacements upon relaxation from the relaxed stoichiometric supercell reported in Table 7. Indeed, while in P1 the largest displacements are obtained for the two reduced Ti^{3+} atoms (Ti_1 and Ti_2), a much more pronounced atomic reorganization is obtained in the P4 case. In particular, while the Ti_1 and Ti_2 atoms still relax substantially, the two-fold coordinated surface O_9 atom displays very large displacements along the [−101] and [101] directions and migrates to fill the initial V_O lattice position (see Fig. 8). This effect has already been mentioned by Ha and Alexandrova [34], although it was only obtained with DFT+U approaches and specific values of the U parameter.

The spin densities computed for the P1 and P4 cases and reported in Figs. 7 and 8 confirm these trends, with spin densities localizing almost exclusively on the two nearest neighbors Ti sites to the V_O, as indicated by the absolute values of the magnetic moments of these two atoms of at least 0.83 μ_B in all cases. Like in the bulk case, the spin contamination of the T spin state was found to be small (below 0.01), but close to 1.00 for the S spin state. The computed average offsets from the CBM of the

Ti^{3+} contributions to the DOS for the two most stable positions found (P1 and P4) are in excellent agreement with the experimental PES value for anatase (101) surface samples of 1.3 eV [65], as well as the 1.3 eV value reported by Deák et al. at the HSE06/PAW level [65] in the S spin state. In addition, we note a larger delocalization of the defect levels in the DOS in the subsurface P4 case than in the P1 case, in line with a recent publication [37], as well as the HOCO plots presented in Fig. 6, where this CO is found more delocalized when the defective site is P4 than P1.

Conclusions

In this work, five exchange-correlation functionals (PBE and four hybrids PBE0, B3LYP, B3PW, and HSE06), combined with two dispersion models (D2 and D3) have first been considered to investigate the structural and electronic properties of stoichiometric bulk TiO_2 anatase, taking into account both ECP and AE basis sets within a GTO-based periodic formalism. Although the best results have been obtained with the HSE06 functional including additional dispersive interactions (with D2 or D3 contributions) and AE basis sets, an AE//ECP computational strategy was found to be a suitable tradeoff between accuracy and computational cost. Indeed, the investigation of the defective bulk system with one V_O both in singlet (S) and triplet (T) spin states has proven ECP basis sets to be inadequate for the description of the positions of the two defect levels in the stoichiometric material band gap. When considering the HSE06-D2 AE//ECP computational strategy however, a very good agreement with experimental PES data indicating an offset of about 1.1 eV from the CBM for these levels could be obtained, with computed values of 0.90 and 0.98 eV in the S and T spin states, respectively. Significantly different local structural polaronic distortions around the V_O site between the S and T spin state solutions could be evidenced however, with a larger asymmetry in the T case than in the S one. In both cases, the vacancy creation led to the localization of the two excess electrons on the two first nearest neighbor Ti^{3+} sites and lattice relaxation was found to be small, compared to the substantial local structural modifications around the V_O site.

The same computational strategy was then considered to investigate a defective anatase (101) surface, taking into account nine different vacancy positions and both S and T spin states. In all cases, computed vacancy formation energies were found to be lower than in the bulk case, and significantly different values were obtained between the different positions. The surface twofold coordinated oxygen site was found to be the most stable one, while the surface threefold coordinated oxygen site was found to be the least stable one, in agreement with recently published theoretical works with hybrid functionals. For the most stable sites found, the computed offsets of the defect levels positions from the CBM were found to be in excellent agreement with the 1.3 eV value obtained experimentally by PES, with computed values ranging between 1.1 and 1.3 eV. While the two first nearest neighbor Ti^{3+} sites where the excess electrons localize relax substantially upon vacancy creation, significant O atoms migration up to the initial vacancy site were also found in some cases, in excellent agreement with other hybrid functional-based computational works.

Overall therefore, the very good agreement obtained with available experimental data regarding the offsets from the CBM of the defect levels positions both for the bulk and the (101) surface of TiO_2 anatase is encouraging for the application of the proposed HSE06-D2 AE//ECP computational strategy to TiO_2 surface-related processes such as TiO_2-based photocatalysis where oxygen vacancies are known to play a key role.

Supplementary Information The online version contains supplementary material available at https://doi.org/10.1007/s00894-023-05584-7.

Acknowledgements The authors acknowledge the use of computational resources at Très Grand Centre de Calcul (TGCC) provided by GENCI (project A0050810135).

Author contributions Z.W. prepared the first version of the article and all corresponding figures and tables. F. L. revised the article and supervised the work.

Funding Z.W. has been awarded a PhD grant from the Chinese Scholarship Council (CSC).

Data availability All numerical data available from the corresponding author upon request.

Declarations

Competing interests The authors declare no competing interests.

References

1. Pantelides ST (1978) The electronic structure of impurities and other point defects in semiconductors. Rev Mod Phys 50:797–858. https://doi.org/10.1103/RevModPhys.50.797
2. Queisser HJ, Haller EE (1998) Defects in semiconductors: some fatal, some vital. Science 281:945–950. https://doi.org/10.1126/science.281.5379.945
3. Ganduglia-Pirovano MV, Hofmann A, Sauer J (2007) Oxygen vacancies in transition metal and rare earth oxides: current state of understanding and remaining challenges. Surf Sci Rep 62:219–270. https://doi.org/10.1016/j.surfrep.2007.03.002
4. Pacchioni G (2008) Modeling doped and defective oxides in catalysis with density functional theory methods: room for

improvements. J Chem Phys 128:182505. https://doi.org/10.1063/1.2819245
5. Gunkel F, Christensen DV, Chen YZ, Pryds N (2020) Oxygen vacancies: the (in) visible friend of oxide electronics. Appl Phys Lett 116:120505. https://doi.org/10.1063/1.5143309
6. Hwang HY, Iwasa Y, Kawasaki M et al (2012) Emergent phenomena at oxide interfaces. Nat Mater 11:103–113. https://doi.org/10.1038/nmat3223
7. Yim CM, Pang CL, Thornton G (2010) Oxygen vacancy origin of the surface band-gap state of TiO_2 (110). Phys Rev Lett 104:036806. https://doi.org/10.1103/PhysRevLett.104.036806
8. Padervand M, Salari H, Ahmadvand S, Gholami MR (2012) Removal of an organic pollutant from waste water by photocatalytic behavior of AgX/TiO_2 loaded on mordenite nanocrystals. Res Chem Intermed 38:1975–1985. https://doi.org/10.1007/s11164-012-0519-8
9. Wang Y, Liu L, Xu L et al (2013) Ag/TiO_2 nanofiber heterostructures: Highly enhanced photocatalysts under visible light. J Appl Phys 113:174311. https://doi.org/10.1063/1.4803844
10. Divya S, Thankappan A, Vallabhan CPG et al (2014) Electrolyte/photoanode engineered performance of TiO_2 based dye sensitised solar cells. J Appl Phys 115:064501. https://doi.org/10.1063/1.4864021
11. Salaoru I, Prodromakis T, Khiat A, Toumazou C (2013) Resistive switching of oxygen enhanced TiO_2 thin-film devices. Appl Phys Lett 102:013506. https://doi.org/10.1063/1.4774089
12. Elahifard MR, Rahimnejad S, Pourbaba R et al (2011) Photocatalytic mechanism of action of apatite-coated Ag/AgBr/TiO_2 on phenol and *Escherichia coli* and *Bacillus subtilis* bacteria Under Various Conditions. Prog React Kinet Mech 36:38–52. https://doi.org/10.3184/146867810X12925913885187
13. Elahifard M, Heydari H, Behjatmanesh-Ardakani R et al (2020) A computational study on the effect of Ni impurity and O-vacancy on the adsorption and dissociation of water molecules on the surface of anatase (101). J Phys Chem Solids 136:109176. https://doi.org/10.1016/j.jpcs.2019.109176
14. Wu J-M, Chen C-J (1990) Effect of powder characteristics on microstructures and dielectric properties of (Ba, Nb)-doped titania ceramics. J Am Ceram Soc 73:420–424. https://doi.org/10.1111/j.1151-2916.1990.tb06528.x
15. Siefering KL, Griffin GL (1990) Growth Kinetics of CVD TiO_2: influence of Carrier Gas. J Electrochem Soc 137:1206–1208. https://doi.org/10.1149/1.2086632
16. Etacheri V, Seery MK, Hinder SJ, Pillai SC (2011) Oxygen rich titania: a dopant free, high temperature stable, and visible-light active anatase photocatalyst. Adv Funct Mater 21:3744–3752. https://doi.org/10.1002/adfm.201100301
17. Schaub R, Thostrup P, Lopez N et al (2001) Oxygen vacancies as active sites for water dissociation on rutile TiO_2 (110). Phys Rev Lett 87:266104. https://doi.org/10.1103/PhysRevLett.87.266104
18. Fukui K, Onishi H, Iwasawa Y (1997) Atom-resolved image of the TiO_2 (110) surface by noncontact atomic force microscopy. Phys Rev Lett 79:4202–4205. https://doi.org/10.1103/PhysRevLett.79.4202
19. Wendt S, Schaub R, Matthiesen J et al (2005) Oxygen vacancies on TiO_2(110) and their interaction with H_2O and O_2: a combined high-resolution STM and DFT study. Surf Sci 598:226–245. https://doi.org/10.1016/j.susc.2005.08.041
20. Hagfeldt A, Graetzel M (1995) Light-induced redox reactions in nanocrystalline systems. Chem Rev 95:49–68. https://doi.org/10.1021/cr00033a003
21. Watanabe T, Nakajima A, Wang R et al (1999) Photocatalytic activity and photoinduced hydrophilicity of titanium dioxide coated glass. Thin Solid Films 351:260
22. Sumita T, Yamaki T, Yamamoto S, Miyashita A (2002) Photo-induced surface charge separation of highly oriented TiO_2 anatase and rutile thin films. Appl Surf Sci 200:21
23. Cheng H, Selloni A (2009) Surface and subsurface oxygen vacancies in anatase TiO2 and differences with rutile. Phys Rev B 79:092101. https://doi.org/10.1103/PhysRevB.79.092101
24. Roldán A, Boronat M, Corma A, Illas F (2010) Theoretical confirmation of the enhanced facility to increase oxygen vacancy concentration in TiO_2 by iron doping. J Phys Chem C 114:6511–6517. https://doi.org/10.1021/jp911851h
25. Deák P, Kullgren J, Frauenheim T (2014) Polarons and oxygen vacancies at the surface of anatase TiO_2: Polarons and oxygen vacancies at the surface of anatase TiO_2. Phys Status Solidi RRL - Rapid Res Lett 8:583–586. https://doi.org/10.1002/pssr.201409139
26. Mori-Sánchez P, Cohen AJ, Yang W (2008) Localization and delocalization errors in density functional theory and implications for band-gap prediction. Phys Rev Lett 100:146401. https://doi.org/10.1103/PhysRevLett.100.146401
27. Na-Phattalung S, Smith MF, Kim K et al (2006) First-principles study of native defects in anatase TiO_2. Phys Rev B 73:125205. https://doi.org/10.1103/PhysRevB.73.125205
28. Osorio-Guillén J, Lany S, Zunger A (2008) Atomic control of conductivity versus ferromagnetism in wide-gap oxides via selective doping: V, Nb, Ta in Anatase TiO_2. Phys Rev Lett 100:036601. https://doi.org/10.1103/PhysRevLett.100.036601
29. Finazzi E, Di Valentin C, Pacchioni G, Selloni A (2008) Excess electron states in reduced bulk anatase TiO_2: comparison of standard GGA, GGA+U, and hybrid DFT calculations. J Chem Phys 129:154113. https://doi.org/10.1063/1.2996362
30. Di Valentin C, Pacchioni G, Selloni A (2006) Electronic structure of defect states in hydroxylated and reduced rutile TiO_2 (110) Surfaces. Phys Rev Lett 97:166803. https://doi.org/10.1103/PhysRevLett.97.166803
31. Di Valentin C, Pacchioni G, Selloni A (2009) Reduced and n-type doped TiO_2 : nature of Ti^{3+} species. J Phys Chem C 113:20543–20552. https://doi.org/10.1021/jp9061797
32. Yamamoto T, Ohno T (2012) A hybrid density functional study on the electron and hole trap states in anatase titanium dioxide. Phys Chem Chem Phys 14:589–598. https://doi.org/10.1039/C1CP21547G
33. Li H, Guo Y, Robertson J (2015) Calculation of TiO_2 surface and subsurface oxygen vacancy by the screened exchange functional. J Phys Chem C 119:18160–18166. https://doi.org/10.1021/acs.jpcc.5b02430
34. Ha M-A, Alexandrova AN (2016) Oxygen vacancies of anatase(101): extreme sensitivity to the density functional theory method. J Chem Theory Comput 12:2889–2895. https://doi.org/10.1021/acs.jctc.6b00095
35. Aryasetiawan F, Gunnarsson O (1998). The GW method. Rep Prog Phys 61:237–312. https://doi.org/10.1088/0034-4885/61/3/002
36. Malashevich A, Jain M, Louie SG (2014) First-principles DFT + GW study of oxygen vacancies in rutile TiO_2. Phys Rev B 89:075205. https://doi.org/10.1103/PhysRevB.89.075205
37. Hao Y, Chen T, Zhang X et al (2019) Ti-Ti σ bond at oxygen vacancy inducing the deep defect level in anatase TiO_2 (101) surface. J Chem Phys 150:224702. https://doi.org/10.1063/1.5108595
38. Cheng H, Selloni A (2009) Energetics and diffusion of intrinsic surface and subsurface defects on anatase TiO_2(101). J Chem Phys 131:054703. https://doi.org/10.1063/1.3194301
39. Heyd J, Scuseria GE, Ernzerhof M (2003) Hybrid functionals based on a screened Coulomb potential. J Chem Phys 118:8207–8215. https://doi.org/10.1063/1.1564060

40. Krukau AV, Vydrov OA, Izmaylov AF, Scuseria GE (2006) Influence of the exchange screening parameter on the performance of screened hybrid functionals. J Chem Phys 125:224106. https://doi.org/10.1063/1.2404663
41. Thomas AG, Flavell WR, Mallick AK et al (2007) Comparison of the electronic structure of anatase and rutile TiO_2 single-crystal surfaces using resonant photoemission and x-ray absorption spectroscopy. Phys Rev B 75:035105. https://doi.org/10.1103/PhysRevB.75.035105
42. Morgan BJ, Watson GW (2007) A DFT+U description of oxygen vacancies at the TiO_2 rutile (110) surface. Surf Sci 601:5034–5041. https://doi.org/10.1016/j.susc.2007.08.025
43. Liechtenstein AI, Anisimov VI, Zaanen J (1995) Density-functional theory and strong interactions: orbital ordering in Mott-Hubbard insulators. Phys Rev B 52:R5467–R5470. https://doi.org/10.1103/PhysRevB.52.R5467
44. Dudarev SL, Botton GA, Savrasov SY et al (1998) Electron-energy-loss spectra and the structural stability of nickel oxide: An LSDA+U study. Phys Rev B 57:1505–1509. https://doi.org/10.1103/PhysRevB.57.1505
45. Dovesi R, Erba A, Orlando R et al (2018) Quantum-mechanical condensed matter simulations with CRYSTAL. WIREs Comput Mol Sci 8:e1360. https://doi.org/10.1002/wcms.1360
46. Dovesi R, Pascale F, Civalleri B et al (2020) The CRYSTAL code, 1976–2020 and beyond, a long story. J Chem Phys 152:204111. https://doi.org/10.1063/5.0004892
47. Adamo C, Barone V (1999) Toward reliable density functional methods without adjustable parameters: The PBE0 model. J Chem Phys 110:6158–6170. https://doi.org/10.1063/1.478522
48. Perdew JP, Burke K, Ernzerhof M (1996) Generalized Gradient Approximation Made Simple. Phys Rev Lett 77:3865–3868. https://doi.org/10.1103/PhysRevLett.77.3865
49. Yanai T, Tew DP, Handy NC (2004) A new hybrid exchange–correlation functional using the Coulomb-attenuating method (CAM-B3LYP). Chem Phys Lett 393:51–57. https://doi.org/10.1016/j.cplett.2004.06.011
50. Becke AD (1993) Density-functional thermochemistry. III. The role of exact exchange. J Chem Phys 98:5648–5652. https://doi.org/10.1063/1.464913
51. Grimme S (2006) Semiempirical GGA-type density functional constructed with a long-range dispersion correction. J Comput Chem 27:1787–1799. https://doi.org/10.1002/jcc.20495
52. Grimme S, Antony J, Ehrlich S, Krieg H (2010) A consistent and accurate ab initio parametrization of density functional dispersion correction (DFT-D) for the 94 elements H-Pu. J Chem Phys 132:154104. https://doi.org/10.1063/1.3382344
53. Durand P, Barthelat J-C (1975) A theoretical method to determine atomic pseudopotentials for electronic structure calculations of molecules and solids. Theor Chim Acta 38:283–302. https://doi.org/10.1007/BF00963468
54. Barthelat JC, Durand P, Serafini A (1977) Non-empirical pseudopotentials for molecular calculations. Mol Phys 33:159–180. https://doi.org/10.1080/00268977700103141
55. Berthelat J, Durand P (1978) Recent progress of pseudopotential methods in quantum chemistry. Gazzetta Chim Ital 108:225–236
56. Labat F, Ciofini I, Adamo C (2012) Revisiting the importance of dye binding mode in dye-sensitized solar cells: a periodic viewpoint. J Mater Chem 22:12205–12211. https://doi.org/10.1039/C2JM31119D
57. Labat F, Baranek P, Domain C et al (2007) Density functional theory analysis of the structural and electronic properties of TiO_2 rutile and anatase polytypes: Performances of different exchange-correlation functionals. J Chem Phys 126:154703. https://doi.org/10.1063/1.2717168
58. Dovesi R, Saunders VR, Roetti C, Orlando R, Zicovich-Wilson CM, Pascale F, Civalleri B, Doll K, Harrison NM, Bush IJ, D'Arco P, Llunell M, Causà M, Noël Y, Maschio L, Erba A, Rerat M, Casassa S (2017) CRYSTAL17 User's Manual, University of Torino, Torino
59. Monkhorst HJ, Pack JD (1976) Special points for Brillouin-zone integrations. Phys Rev B 13:5188–5192. https://doi.org/10.1103/PhysRevB.13.5188
60. Sanches FF, Mallia G, Liborio L et al (2014) Hybrid exchange density functional study of vicinal anatase TiO_2 surfaces. Phys Rev B 89:245309. https://doi.org/10.1103/PhysRevB.89.245309
61. Burdett JK, Hughbanks T, Miller GJ et al (1987) Structural-electronic relationships in inorganic solids: powder neutron diffraction studies of the rutile and anatase polymorphs of titanium dioxide at 15 and 295 K. J Am Chem Soc 109:3639–3646. https://doi.org/10.1021/ja00246a021
62. Tang H, Berger H, Schmid PE et al (1993) Photoluminescence in TiO_2 anatase single crystals. Solid State Commun 87:847–850. https://doi.org/10.1016/0038-1098(93)90427-O
63. Labat F, Baranek P, Adamo C (2008) Structural and electronic properties of selected rutile and anatase TiO_2 surfaces: an ab Initio Investigation. J Chem Theory Comput 4:341–352. https://doi.org/10.1021/ct700221w
64. Setvin M, Schmid M, Diebold U (2015) Aggregation and electronically induced migration of oxygen vacancies in TiO_2 anatase. Phys Rev B 91:195403. https://doi.org/10.1103/PhysRevB.91.195403
65. Jackman MJ, Deák P, Syres KL, et al (2014) Observation of vacancy-related polaron states at the surface of anatase and rutile TiO_2 by high-resolution photoelectron spectroscopy. https://doi.org/10.48550/arXiv.1406.3385

Publisher's note Springer Nature remains neutral with regard to jurisdictional claims in published maps and institutional affiliations.

Springer Nature or its licensor (e.g. a society or other partner) holds exclusive rights to this article under a publishing agreement with the author(s) or other rightsholder(s); author self-archiving of the accepted manuscript version of this article is solely governed by the terms of such publishing agreement and applicable law.